



X-ray Computed Tomography for Wall Thickness Evaluation and Through-Hole Detection in Additively Manufactured Hollow Lattice Structures

Ibon Holgado¹ · Naiara Ortega² · José A. Yagüe-Fabra³ · Soraya Plaza² · Herminso Villarraga-Gómez⁴

Received: 8 April 2025 / Accepted: 31 August 2025
© The Author(s) 2025

Abstract

This study investigates the trade-off between minimizing wall thickness and through-hole formation in AISi10Mg thin hollow lattice structures produced via laser powder bed fusion. X-ray computed tomography (XCT) is employed as a metrological tool to evaluate the effects of laser linear energy density (LED) across conditions ranging from under-melting to over-melting using a single laser track strategy. An XCT-based algorithm is developed for automated through-hole detection, providing quantitative data on through-hole count and size. The algorithm's capability is evaluated through leakage tests. The substitution method, adapted from ISO 15530–3 for tactile coordinate measuring machines (CMM), is employed to assess XCT measurement uncertainty for hollow lattice dimensions. As a new addition to the conventional substitution method, the effects of high-density data generated by XCT are assessed against the calibrated diameters obtained from low-density CMM data and used for the calculation of wall thickness. Experimental results show that under-melting conditions can produce wall thicknesses of 0.135 mm to 0.212 mm, with an exponential increase in through-hole formation as LED decreases. A linear relationship between LED and wall thickness is observed, enabling identification of optimal parameters for producing defect-free thin-walled structures.

Keywords Hollow lattice · Additive manufacturing · X-ray computed tomography · Measurement uncertainty · Through-hole

1 Introduction

Natural selection has driven the evolution of lightweight biological structures with unique physical and mechanical properties, enabling adaptation to varied environmental conditions [1]. Hollow structures in nature, such as avian bones and bamboo stems, illustrate convergent evolution

by optimizing fluid transport and mechanical strength. The same architectural principle has also been extensively adopted in structural design across various engineering fields, where hollow circular sections offer superior load-bearing efficiency compared to solid beams of equal mass, optimizing mechanical strength while minimizing material usage, as exemplified in Fig. 1a [2, 3]. Lattice structures, known for their energy absorption and lightweight properties, are also commonly found in natural systems and are increasingly integrated into advanced design applications, as shown in Fig. 1b [4]. Lattice structures enable mesoscale geometric modifications to control mechanical performance without requiring changes at the microstructural level [5].

The integration of hollow and lattice structures has recently become feasible with advancements in Additive Manufacturing (AM) technology. Current industrial demands prioritize optimized designs, such as hollow and lattice configurations, to address thermal management challenges in next-generation components [11]. Hollow lattice designs enable a significant increase in surface area,

✉ Ibon Holgado
ibon.holgado@ehu.eus

¹ Aeronautics Advanced Manufacturing Center, CFAA (UPV/EHU), Bizkaia Technology Park, Building 202, 48170 Zamudio, Spain

² Bilbao School of Engineering, UPV/EHU, Plaza Torres Quevedo 1, 48013 Bilbao, Spain

³ I3A, University of Zaragoza, María de Luna 3, 50018 Zaragoza, Spain

⁴ Carl Zeiss Industrial Quality Solutions, LLC, Wixom, MI, USA

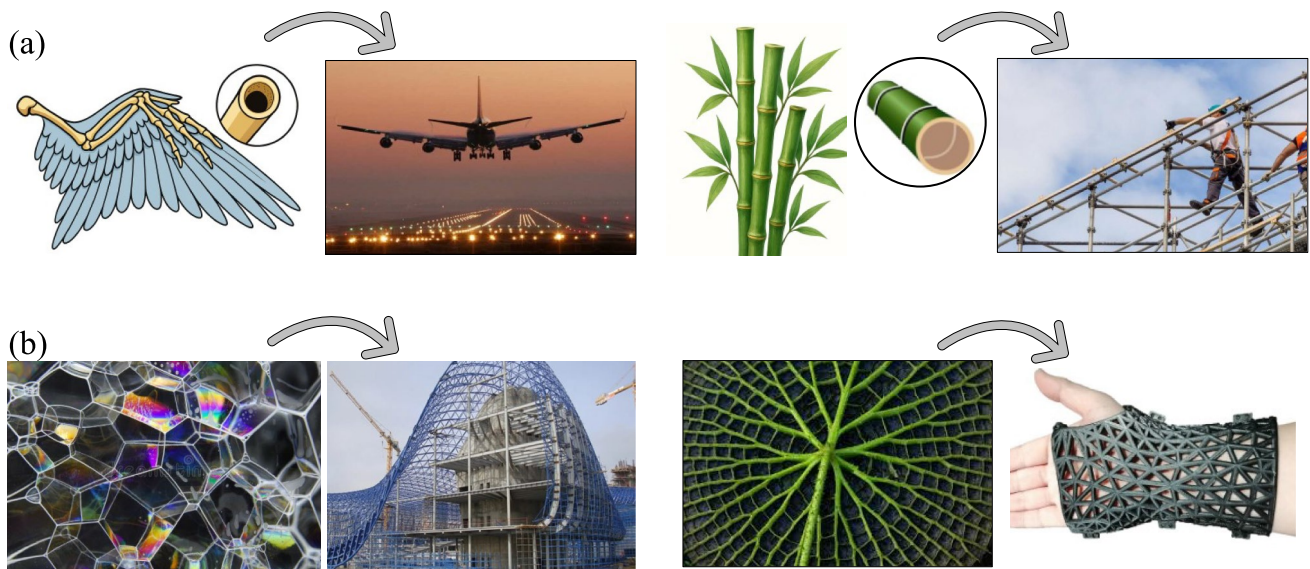


Fig. 1 (a) Examples of hollow structures in nature and engineering: avian hollow bones, aircraft structure [2], bamboo stems and hollow tubular scaffolding used in civil construction [6]. (b) Examples of lattice architectures in biological and engineered systems: bubble-

derived stochastic cellular structures [7], lattice structural envelopes in modern buildings [8], the ribbed support network of Victoria amazonica (giant water lily) [9], and orthopedic implants incorporating lattice frameworks [10]

enhancing both convective and conductive heat transfer efficiency, which is critical for thermal management in high-performance applications [12]. Moreover, the hollow sections facilitate concurrent fluid flow through multiple channels, an innovation unattainable with solid struts, thereby improving overall heat dissipation capabilities [13]. In addition, recent studies have shown that hollow-strut metal lattice materials can exhibit superior mechanical performance compared to their solid-strut counterparts at equivalent relative densities, further underscoring the potential of hollow lattice structures [14]. Among materials commonly used for advanced AM applications, aluminum alloys have emerged as a key choice due to their high strength, low density, thermal conductivity, and corrosion resistance [15].

Despite progress in AM techniques, including laser powder bed fusion (PBF-LB), the most widely adopted method for industrial applications, manufacturing thin-walled AlSi10Mg components remains challenging [16]. Aluminum's high reflectivity and thermal conductivity necessitate increased laser energy, often leading to unstable melt pools and a higher likelihood of defect formation, particularly in thin sections fabricated with single laser scan paths [17]. Achieving consistent thin wall thickness with dimensional accuracy and without through-holes remains a significant challenge in PBF-LB processes due to the high sensitivity of energy input and melt pool stability. Nayak et al. emphasized the importance of balancing over-melting and under-melting conditions in single laser track strategies to optimize submillimeter wall thickness manufacturing, though their effect on through

holes' generation is not well understood [18]. Specifically, under-melting linear energy densities were found to reduce laser single track produced wall thickness but significantly increased the probability of lack-of-fusion (LoF) defects and leakage risks [19].

Recent literature has highlighted the critical role of LoF defects as a dominant mechanism contributing to through-hole formation in thin-walled AM structures. Snow et al. demonstrated that LoF defects can be directly caused by the presence of spatter particles, which obstruct powder melting during laser exposure. Their study provided quantitative spatial correlations between in situ monitoring spatter maps and internal porosity detected via X-ray computed tomography (XCT), confirming that the orientation of the laser path influences both spatter behavior and the resulting porosity [20]. Schwerz et al. further showed that re-deposited spatter particles are strongly associated with the occurrence of large LoF defects, particularly in areas near the gas outlet. Their findings also indicate that flaw distribution varies significantly even when using identical process parameters, highlighting the influence of gas flow and local part positioning [21]. Similarly, Bonato et al. explored analytical and machine learning-based defect prediction approaches based on in-process monitoring data. Their findings demonstrated that reliable detection of LoF defects, particularly those exceeding 80 μm , requires multi-layer process history analysis, as these flaws can propagate vertically across several layers. This behavior is particularly critical in thin-walled regions comprising only one or few layers, where a single defect may result in full wall penetration [22].

In addition to LoF defects, residual stresses and thermally induced cracking have been identified as critical phenomena that may contribute to through-hole formation in thin-walled PBF-LB components. The high thermal gradients and rapid solidification inherent to PBF-LB processes lead to tensile residual stresses near the surface, which can reach magnitudes close to the material's yield strength and vary significantly with build orientation [23]. These stresses can cause localized warping or crack initiation, especially in thin geometries where mechanical constraint is limited.

While such cracks are often shallow and not detectable with non-destructive testing (NDT) methods, in very thin walls they may propagate through the entire section, creating unintended through holes that compromise component hermeticity. This effect is exacerbated in high-conductivity alloys like AlSi10Mg, where the absence of substrate preheating further increases cooling rates and crack susceptibility [24]. Moreover, the spatial distribution of residual stresses can be influenced by process parameters, energy density, scan strategy, and part positioning on the build plate, reinforcing the importance of understanding these effects when assessing through-hole risks [25].

In the literature Industrial XCT has proven to be an effective NDT technique for dimensional quality control of complex-shaped AM parts [26]. While XCT is suitable for hollow thin walls dimensional measurements and porosity quantitative evaluation, its application in automated through-hole detection and traceable wall thickness measurements for thin-walled structures is underdeveloped. Current literature efforts frequently rely on manual analysis for through-holes detection, leading to variability and inconsistencies in reported findings. Moreover, the lack of standardized measurement protocols for uncertainty quantification, an essential aspect for evaluating the reliability of dimensional inspection results, underscores the need for further research to ensure accurate and traceable measurements of hollow wall thicknesses [27].

This study explores the trade-off between minimizing wall thickness and the through-hole formation probability in AlSi10Mg hollow lattice structures produced via PBF-LB. Using XCT as a metrological tool, the effects of laser energy density are analyzed across a parameter space ranging from under-melting to over-melting using a single laser track strategy. A novel hollow lattice design is developed to enable the substitution method, adapted from coordinate metrology standards, for assessing dimensional measurement uncertainties in XCT. Additionally, a novel XCT-based algorithm is introduced for automated through-hole detection, providing quantitative data on through-hole count and size. The findings provide valuable insights for optimizing PBF-LB parameters to produce thin-walled components with controlled leakage characteristics.

2 Materials and Methods

2.1 Material Measure Description

Two different hollow lattice-structured test objects (hereafter referred to as the material measures) made of AlSi10Mg were fabricated using plasma-atomized powder (15–53 μm) on a RenAM 500Q PBF-LB machine, using a laser spot size of 80 μm . The unit cell, measuring $8 \times 8 \times 8 \text{ mm}^3$, was arranged in a $3 \times 3 \times 4$ lattice configuration with hollow struts of 2.2 mm outer diameter. The design used a body-centered cubic configuration with z-axis reinforcement (BCCz), a stretch-dominated configuration widely recognized for its favorable mechanical performance and increasingly adopted in hollow-walled lattice applications [28]. This z-axis reinforcement consisted of vertical hollow struts across the 16 nodal points of the structure, enabling consistent wall thickness measurements along hollow strut axes normal to the build plane. The first material measure (MM1) featured a uniform nominal wall thickness of 0.3 mm and was fabricated using a single laser scan path strategy. To investigate the effect of energy input on manufacturing quality under single laser track conditions, the linear energy density (LED) was defined according to Eq. 1 [29]:

$$LED = \frac{P}{V} \quad (1)$$

where P is the laser power and V is the scanning speed.

LED was systematically varied across six (4 mm height) regions to evaluate conditions ranging from under-melting to over-melting (Fig. 2a). The objective of MM1 was to evaluate the wall thickness obtained and the occurrence of through-holes at each tested LED values. In this study, a through-hole is defined as any continuous open defect fully penetrating the wall, connecting the internal and external surfaces, regardless of its origin or geometry.

The second material measure (MM2) featured a uniform wall thickness of 0.7 mm, a thickness sufficient to ensure the absence of through-holes and was manufactured using 0.336 J/mm LED. MM2 incorporated a semi-cylindrical hollow feature with a flat surface spanning the entire length of the structure (Fig. 2b). This feature contained CAD-designed through-holes as cylinders with varying diameters, serving as controlled leakage points. These intentional CAD-designed holes facilitated direct comparison between XCT-based detection and leakage test results, allowing for evaluation of the detection method while establishing a threshold for XCT minimum through-hole size detectability.

To enable leakage testing, pneumatic connection tubes were integrated at both ends of the material measures where the hollow lattice network converges.

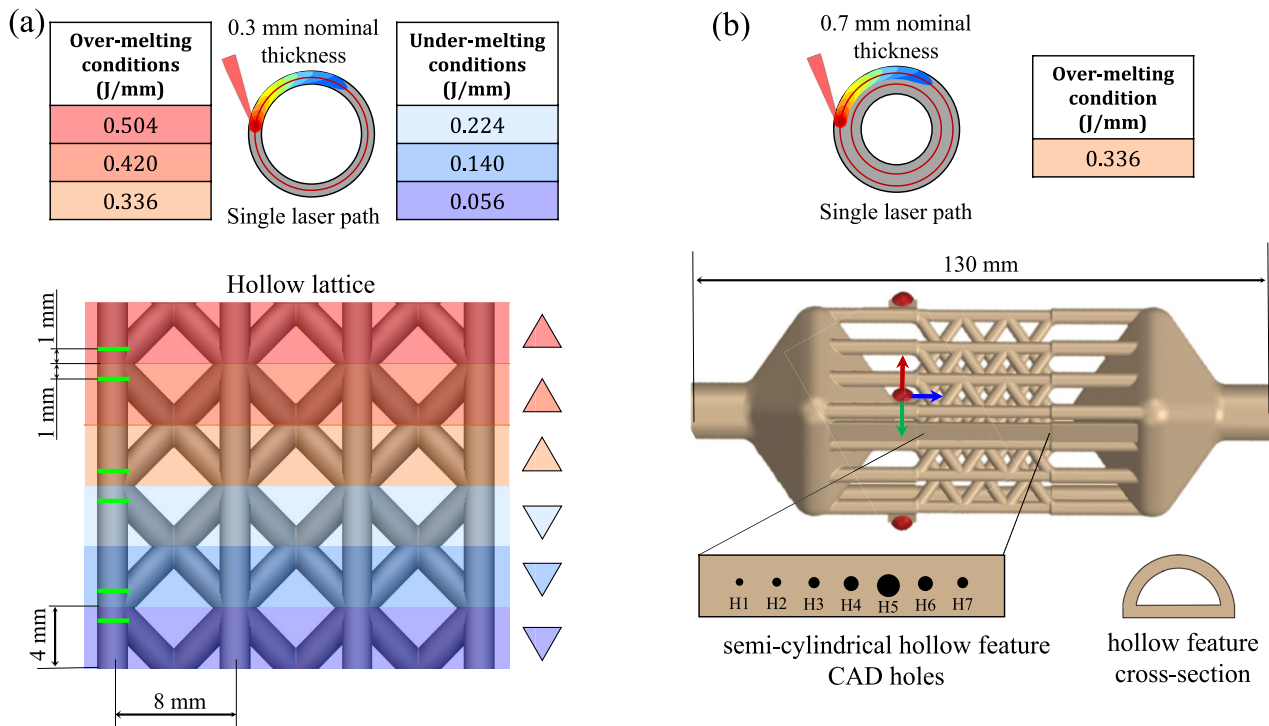


Fig. 2 (a) LED values assigned to each region of MM1, including unit cell dimensions, distribution of LED regions, and corresponding measurement locations. (b) Schematic of MM2 illustrating the semi-

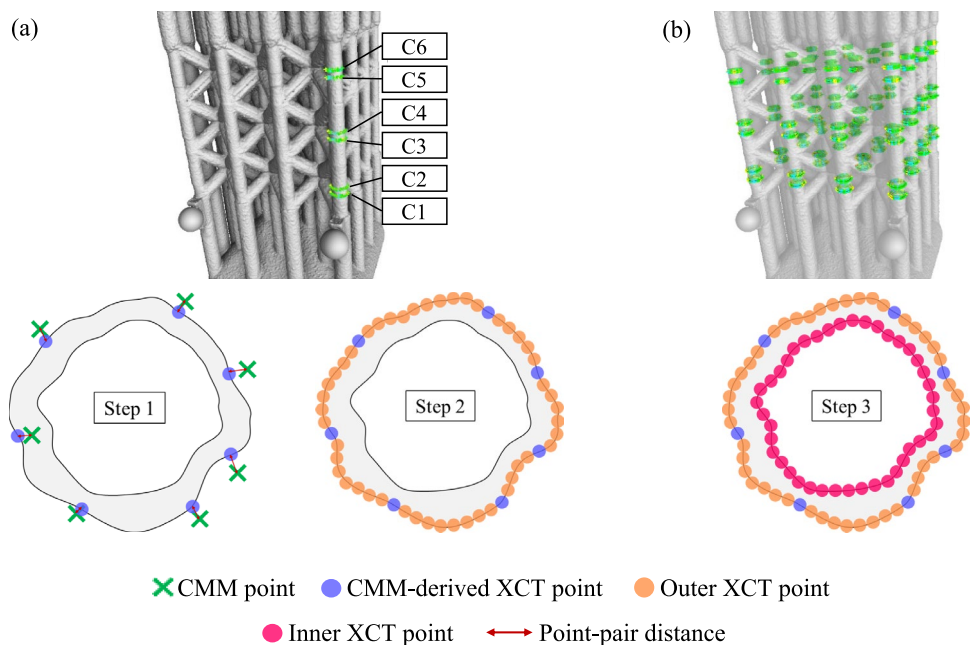
cylindrical hollow feature with embedded CAD-designed through-holes and pneumatic connection tubes

2.2 Material Measure Calibration

Outer diameter measurements were calibrated on the most accessible corner hollow strut of MM1 using a ZEISS F-25 multi-sensor CMM (MPE = $(0.25 + L/666)$ μm) housed in

a calibration center, following the procedure outlined in EA-4/02 M:2022 standard [30] and employing the least squares method (Fig. 3a). The expanded calibration measurement uncertainty was 0.005 mm ($k=2$). Six outer diameter measurements were taken at 1 mm intervals above

Fig. 3 Schematic representation of the systematic three-step procedure: (a) Steps 1 and 2 performed on the most accessible corner hollow strut and (b) Step 3 extended to all 16 hollow struts per manufacturing region of MM1



and below the interface zones between the different LED regions, with a single diameter within each of the six regions (refer to Fig. 2a, green color).

The diameters of the CAD-designed through-holes at the surface of the semi-cylindrical feature of MM2 were calibrated using a ZEISS O-Inspect optical sensor on a multi-sensor CMM, also installed in a calibration center. The mean diameter of each CAD-designed hole was determined using least-squares fitting of sensor-acquired points, with an expanded uncertainty of 0.025 mm ($k=2$) per hole, following also the internationally recognized standard EA-4/02 M:2022 for metrological traceability [30]. Further details on the leakage test methodology and CAD-designed holes in MM2 are provided in Section 2.5.

Additionally, three precision-grade ruby spheres (4 mm diameter) were integrated in the material measures to enable XCT scale factor correction (voxel size adjustment) before XCT dimensional measurements and ensure consistent data alignment between XCT and CMM for measurements at identical locations [31]. These spheres were accommodated using an industrial cyanoacrylate adhesive. The three ruby spheres were arranged in a single plane to define a stable XY reference frame for consistent cross-sectional positioning along the Z-axis, which is aligned with the vertical hollow struts. Although spheres configuration does not define a full 3D volumetric frame, it was considered sufficient for 2D slice registration normal to the strut axes, where the critical dimension of interest (wall thickness) lies in the radial direction. The distances between the centers of the ruby spheres were calibrated using a ZEISS F-25 multi-sensor coordinate measuring machine, in a laboratory accredited by ENAC (*Entidad Nacional de Acreditación*, the Spanish national accreditation body), with a maximum permissible error (MPE) of $(0.25 + L/666) \mu\text{m}$, where L denotes the measured length in millimeters. Sphere centers were computed by applying least-squares fitting to the measured surface data. The calibration was also performed in accordance with the EA-4/02 M:2022 guideline, and the expanded uncertainty (U_{MP}) for these distances was determined to be 0.001 mm ($k=2$), in line with the principles of the Guide to the Expression of Uncertainty in Measurement (GUM). Table 1 summarizes the calibrated distances.

2.3 XCT Hollow Lattice Thickness Measurements

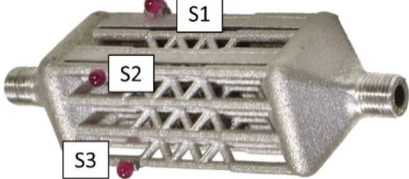
The material measures were scanned using an Rx Solutions EasyTom XL XCT system. To maximize magnification, each material measure was positioned at an optimized distance from the X-ray source, ensuring the entire component remained within the detector's field of view during a full 360° rotation. This setup provided an isotropic voxel size of $44 \mu\text{m}$. The scans were performed at a tube voltage of 180 kV and a filament current of $200 \mu\text{A}$, using 1248 projections and an exposure time of 333 ms. Five scans were performed under controlled temperature conditions to evaluate repeatability. Volumetric data reconstruction was conducted using Rx solution Reconstruction software.

XCT measurement process uncertainty (U_{MP}) was evaluated using the substitution method, following the VDI/VDE 2630–2.1 guideline adapted from ISO 15530–3 for tactile CMMs [32]. The substitution method involves performing multiple XCT scans of the calibrated material measure to evaluate and correct for systematic deviations (b), enabling the estimation of the measurement process uncertainty U_{MP} , as expressed by Eq. 2:

$$U_{MP} = k \cdot \sqrt{u_{cal}^2 + u_{drift}^2 + u_p^2 + u_w^2 + u_b^2}, \quad (2)$$

where k denotes the coverage factor corresponding to a 95% confidence level. The term u_{cal} refers to the standard uncertainty of the reference measurements obtained from the calibration, calculated as $u_{cal} = \frac{U_{cal}}{k_{cal}}$. The u_{drift} component reflects potential geometric changes in the material measure that may occur between calibration and XCT scanning. In this case, u_{drift} was considered negligible, as XCT measurements were conducted immediately following the CMM calibration. The term u_p represents the standard uncertainty related to measurement repeatability. Although ISO 15530–3 prescribes 20 repetitions for tactile CMM evaluations, in this study the number of repetitions was adjusted to five due to the higher cost and time requirements of XCT. To compensate for the reduced number of measurements and maintain a 95% confidence level, a safety factor of 1.4 was applied

Table 1 Distances between centers of the spheres employed for scale factor correction in the material measure. All values are in millimeters (mm)

Distance	Measurement (mm)	U_{MP} ($k=2$)	
C1-C2	27.747	0.001	
C2-C3	24.043	0.001	
C1-C3	39.339	0.001	

[33]. The term u_w accounts for differences in similarity between the calibration and the actual measurement.

Finally, u_b quantifies the uncertainty associated with the correction of b . This was determined from the deviation between the XCT mean values and the calibrated reference values, incorporating thermal effects according to $u_b = \Delta t \cdot u_{\alpha b} \cdot l$. Here, $u_{\alpha b}$ represents the standard uncertainty associated with the material's coefficient of thermal expansion, while Δt accounts for temperature deviations from the reference value of 20 °C, which is the standard for dimensional metrology. Due to the small feature sizes and stable temperature control during scanning, u_b made an insignificant contribution to the overall U_{MP} .

ISO 15530–3 also emphasizes that measurement strategies during calibration and evaluation should remain consistent [34]. However, XCT inherently produces high-density point clouds, whereas CMM relies on a limited number of probing points. This discrepancy in point density, often overlooked in existing literature when adapting the substitution method to XCT, significantly influences contour fitting accuracy and the resulting measurement outcomes. Therefore, as a novel contribution to the conventional substitution method, in this study a systematic three-step procedure was followed to evaluate wall thickness and quantify U_{MP} on MM1, as illustrated in Fig. 3.

Step 1: The six CMM-calibrated diameters were replicated in the XCT data by reapplying the same probing points originally used in the CMM diameter measurements (least squares method). This replication was performed after aligning the XCT dataset to the CMM coordinate system using the three precision-grade ruby spheres. Each CMM probing point was then associated with its corresponding location on the XCT-reconstructed surface

by identifying the closest surface point along the local normal vector. Figure 3, step 1, shows a schematic representation of the closest distance between a CMM point and its corresponding point on the XCT surface, defined as the point-pair distance. The mean point-pair distance was ± 0.005 mm, which is one order of magnitude smaller than the hollow strut diameters, and its minimal contribution is included in the standard uncertainty component of the repeated measurements used to calculate U_{MP} [32]. This step quantified the measurement uncertainties associated with transitioning from CMM to XCT while maintaining the same measured data post-processing. In step 1, u_w contribution was neglected, as both the CMM and XCT measurements were performed at the same locations, ensuring direct comparability with no differences in similarity.

Step 2: The same calibrated diameters were re-measured in XCT data using high-density point data, sampled at 1 μm intervals ($> 10,000$ points), along the surface contours at the same calibrated heights. This step assessed the impact of increased point density on measurement accuracy while maintaining the same measurement instrument. In step 2, in line with established practices in similar studies [33], potential variability (u_w) was incorporated into the repeatability uncertainty (u_p) through repeated measurements. This approach prevents overestimating expanded uncertainty by addressing variability within u_p rather than treating u_w as a separate term.

The complete uncertainty budget for step 1 and step 2 measurements is provided in Table 2, listing the absolute values of all contributing uncertainty sources.

Step 3: Wall thickness was calculated as the radial difference between least-squares-fitted outer and inner circumferences derived from high-density point data. Measurements

Table 2 Step 1 and Step 2 XCT measurements results on the six calibrated outer diameters of the corner hollow strut in the MM1, including uncertainty contributors and expanded uncertainty statements (U_{MP}) $k = 2$. All values not indicated are in millimeters (mm)

	Measured hollow strut	Measurement	b	$u_{cal}(\mu\text{m})$	$u_p(\mu\text{m})$	$U_{MP}(\mu\text{m})$
Step 1 measurement	C1	2.199	0.023	2.0	0.8	4.3
	C2	2.169	0.016	2.0	1.6	5.1
	C3	2.145	0.009	2.0	0.8	4.3
	C4	2.106	0.009	2.0	0.0	4.0
	C5	1.989	−0.021	2.0	0.8	4.3
	C6	2.053	−0.017	2.0	0.8	4.3
Step 2 measurement	C1	2.199	0.023	2.2	0.8	6.3
	C2	2.173	0.012	2.6	0.8	7.5
	C3	2.146	0.008	2.2	0.0	6.1
	C4	2.106	0.009	2.0	0.0	5.6
	C5	1.990	−0.022	2.2	1.4	6.7
	C6	2.053	0.017	2.2	0.8	6.3

were extended beyond the CMM-calibrated corner hollow strut to include all 16 straight hollow struts, with one XCT volume cross-sectional location measured per each of the six distinct LED regions. The calibrated diameters obtained by CMM for the corner hollow strut are shown in Fig. 3a, while the XCT-derived measurements for the 16 straight hollow struts are presented in Fig. 3b.

The similarity required for applying the substitution method is justified, as the outer and inner diameters closely match the calibrated dimensions due to the minimal wall thickness. Wall thickness is derived directly from the difference between these calibrated values. Geometric variations in hollow struts due to manufacturing variability were addressed as the calibrations were performed on the entire range of LED regions.

For each LED region, the representative wall thickness was determined in two steps. First, the wall thickness values from five XCT scan repetitions were averaged for each of the 16 straight hollow struts. Then, the mean of these 16 averaged thickness values and the standard deviation was calculated to define the overall wall thickness for the region.

2.4 XCT-Based Through Holes' Detection Method

A custom Python-based post-processing algorithm was developed to detect through-holes in 3D-reconstructed XCT data. While inspired by the classical flood-fill principle used in image processing, the proposed algorithm incorporates novel logical adaptations specifically tailored to XCT volumetric datasets and the detection of through-holes in hollow structures. Each step of the multi-step flood-fill algorithm is illustrated in Fig. 4.

The through hole detection process begins with the binarization of the XCT dataset into discrete intensity values (0 for background and 255 for material), in this case consistent with the full dynamic range of 8-bit grayscale images, following the application of the local iterative surface determination function in VGSTUDIO MAX 3.4 (Volume Graphics GmbH). This binarization step represents the primary source of uncertainty in the detection process, as it defines the boundary between material and background. The employed local iterative surface determination function, based on local grey value gradients, is widely supported in the literature

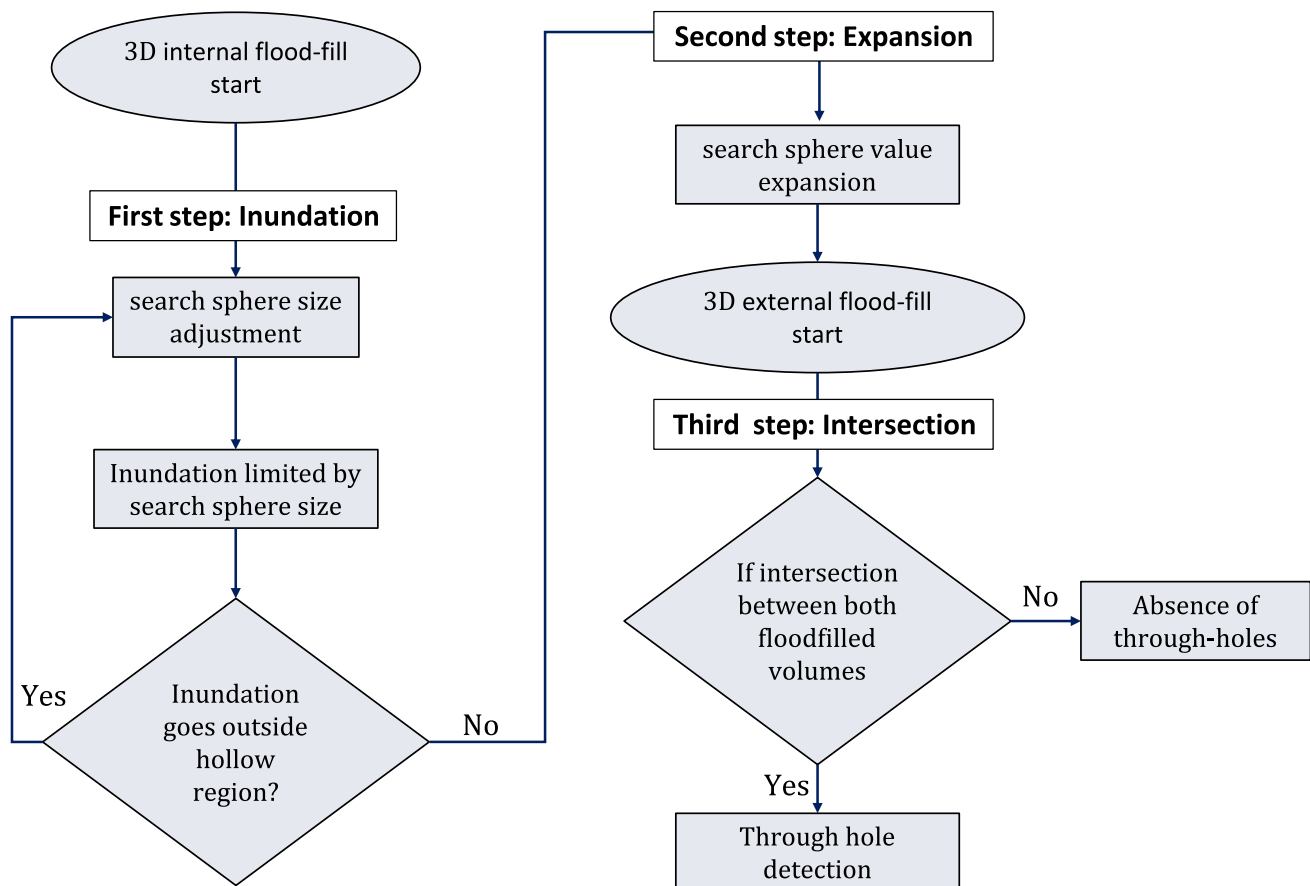


Fig. 4 Schematic representation of the multi-step flood-fill algorithm for automated through-hole detection

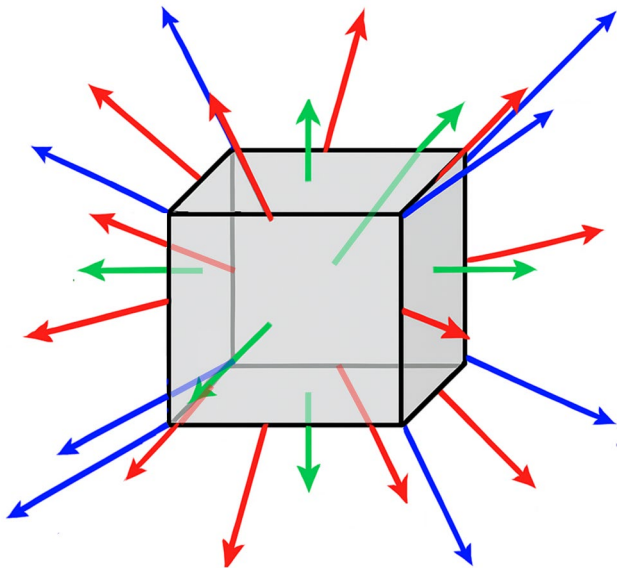


Fig. 5 Voxel connectivity scheme illustrating the 26 flood-fill propagation direction: 6 main directions (green), 12 side directions (red) and 8 diagonal directions (blue)

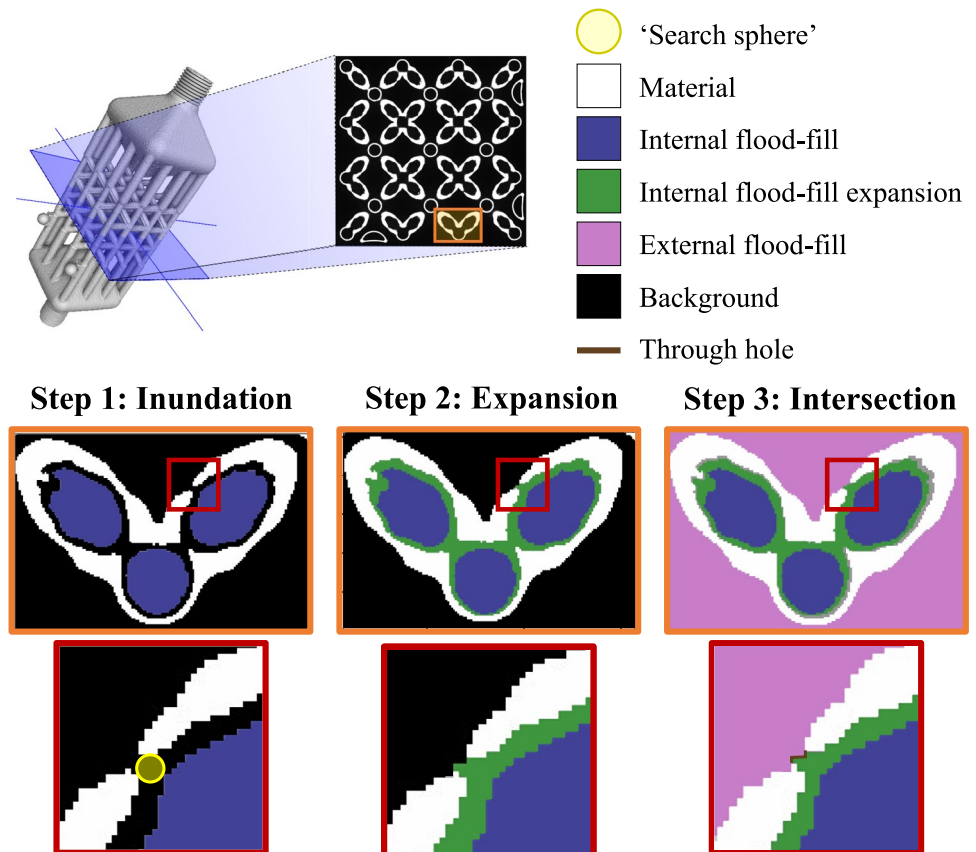
for its superior accuracy and robustness compared to global thresholding methods [35, 36]. However, a detailed uncertainty quantification of its influence on the measurement of specific dimensional and form error characteristics of the

detected through-holes falls outside the scope of the present study. In addition to segmentation, the simply resolution of the XCT system, defined by the selected voxel size of $44\ \mu\text{m}$, also contributes to the overall detection uncertainty. As the voxel size limits the smallest detectable feature, it directly influences the minimum through-hole size that can be reliably identified. Although subvoxel accuracy has been demonstrated in the literature, studies indicate that features must cover at least 4×4 voxels to ensure reliable detection [37, 38]. Accordingly, in this study, only through-holes near or above this minimum size threshold are considered, specifically the CAD-defined through-holes in the MM2 test object, which were used to evaluate the reliability of the proposed XCT-based detection algorithm, as detailed in Section 2.5.

The first step, 'Inundation', illustrated in Fig. 6, involves initiating an internal flood-fill operation from a predefined seed point within the hollow region of the structure. The flood-fill propagates in 26 discrete directions (6 main, 12 side and 8 diagonal directions) across the voxel grid, constrained by a predefined "search sphere" radius. The 26 flood-fill propagation directions are shown in Fig. 5.

This propagation is constrained by a boundary defined as the "search sphere", which sets the maximum distance from the seed point for exploring neighboring voxels. Propagation stops upon encountering material voxels (non-zero intensity values) or reaching the current search radius. To

Fig. 6 Streamlined representation of the multi-step algorithm for automated through-hole detection in MM1



ensure that the flood-fill remains confined within the internal channel and does not extend through external apertures, the radius of the search sphere is increased iteratively. This iterative expansion continues until the flood-fill volume is fully enclosed, meaning no inundation to the exterior occurs. Unlike conventional flood-fill methods, the iterative adjustments to the "search sphere" is critical to ensure the fill remains confined within the hollow channel, avoiding passage through external apertures.

In the second step, 'Expansion', illustrated in Fig. 6, the filled volume is refined by expanding it within the same "search sphere" constraints. This ensures complete occupancy of the hollow channel while maintaining isolation from external apertures.

The third step, 'Intersection', shown in Fig. 6, involves an external flood-fill initiated from outside the hollow structure. This operation propagates in the same 26 directions but uses distinct voxel labels and operates without "search sphere" constraints. Through-holes are identified at the spatial intersection between the internal and external flood-fill volumes. This dual-fill approach, combined with the geometric confinement strategy, enables the algorithm to distinguish true through-holes from surface-breaking pores, near-surface porosity, and incompletely fused sub-surface defects. If no intersection is found, the structure is considered free of through-holes. The key steps of the detection process in MM1 are illustrated in Fig. 6.

The algorithm records the coordinates of intersecting voxels, merging contiguous voxel clusters to define individual through-holes. The voxel count within each cluster is also logged, providing an indicator of the through-hole size.

The computational cost associated with the through-hole detection algorithm is primarily influenced by two factors. First, for a fixed scan volume, the total number of voxels scales cubically with decreasing voxel size, thereby increasing the computational cost due to the greater number of voxel-wise evaluations required. Consequently, finer voxel resolutions lead to proportionally higher processing times. Second, the iterative expansion of the search sphere during

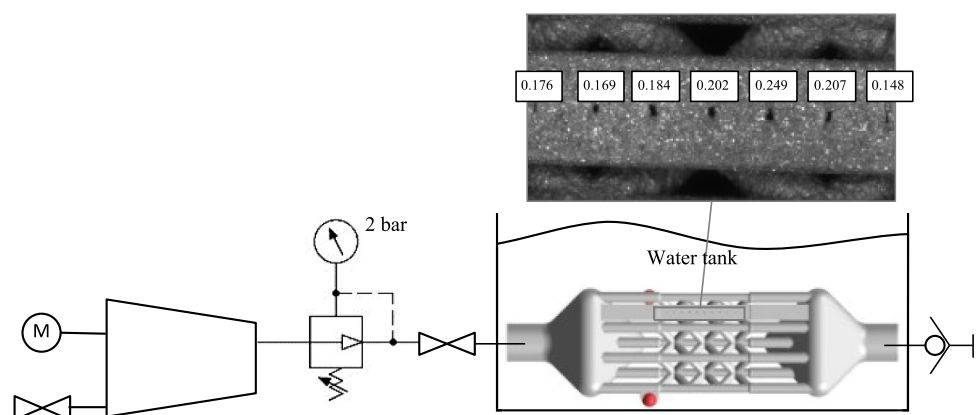
the initial inundation step becomes increasingly demanding in the presence of large through-holes. In such scenarios, multiple iterations are necessary to constrain the flood-fill operation and prevent propagation beyond the hollow channel. Each incremental increase in the search radius substantially enlarges the set of voxels evaluated during propagation, further compounding the computational load. For the 44 μm voxel size used in this study, the algorithm required an average of 6 min 52 s to process each dataset.

2.5 Leakage Test

The material measure MM2 was subjected to a leakage test to evaluate the effectiveness of the XCT-based through-hole detection method, as shown in Fig. 7. A pressure of 2 bar was applied to ensure sufficient sensitivity for through-hole detection while avoiding structural failure of the thin walls. Figure 7 also includes an optical sensor image showing the calibrated through-hole diameters and notable deviations from the nominal cylindrical shapes, attributed to their small size. To ensure compatibility with the XCT detection limit, the smallest CAD-designed through-hole used in the leakage test was selected to approximately match the reliable detection threshold reported in literature. Based on the 44 μm voxel size, a minimum of 4×4 voxels corresponds to a nominal diameter of ~ 0.18 mm. Consequently, the leakage test was not intended to validate sub-voxel features, but to provide experimental qualitative evaluation of the multi-step flood-fill algorithm's reliability near its practical detection threshold.

The test was conducted by fully immersing the material measure in a transparent water tank under standardized high-illumination conditions to ensure clear visibility. The verification zone focused on the CAD-designed through-holes located on the flat surface of the semi-cylindrical feature of MM2. Through-holes were identified by observing air bubbles forming at the leakage points. A high-speed camera system (AOS Technologies), capable of capturing up to 3000 frames per second at full resolution, was employed to record and analyze each leakage point.

Fig. 7 Schematic diagram of the leakage testing setup, showing CAD-designed through-holes on the flat surface of the semi-cylindrical hollow feature of MM2. The numbers in the optical sensor image indicate the calibrated through-hole diameters in millimeters using ZEISS O-Inspect



It is worth noting that the leakage test does not quantify absolute leakage rates but serves solely to qualitatively verify the correspondence between the through-holes detected by XCT and those observable via the high-speed camera.

3 Results and Discussion

3.1 Hollow Lattice Diameter Measurement Uncertainty Using XCT

Figure 8 shows the six calibrated outer diameter measurements of MM1, each performed on a different 4 mm-high LED region (indicated by the colored boxes, with LED values and colors corresponding to Fig. 2a), along with the corresponding U_{MP} values obtained through XCT for the material measure, represented as error bars. Two measurement approaches were analyzed (refer to Fig. 3 a): Step 1, based on the same CMM probe points used during calibration, and Step 2, based on high-density point XCT data, as explained in Section 2.2.

Although standardization efforts are ongoing to define dimensional and geometrical tolerances specifically tailored to AM, this study adopts a conventional tolerance

specification of ± 0.06 mm for hollow lattice strut diameters, as reported in similar literature [33]. According to this specification, the XCT-derived measurement uncertainties obtained from both Step 1 and Step 2 remain within the acceptable tolerance range.

Step 1, which replicates the calibrated CMM probing points, resulted in a maximum U_{MP} of ± 5.1 μm . Step 2, based on high-density point data extracted from the XCT-reconstructed surface, yielded a higher maximum U_{MP} of ± 7.5 μm . This increase in U_{MP} is inherent to the method, as Step 2 involves an additional stage in the traceability path by shifting from calibrated probing points to surface data derived from XCT.

The benefit of high-density point sampling lies in its enhanced surface characterization capability. By using significantly more data points ($> 10,000$), step 2 measurement enables the detection of fine geometrical features, such as local peaks or valleys between sparsely distributed CMM points, which would otherwise remain undetected. Therefore, despite the increased uncertainty, Step 2 provides valuable geometric insight for applications that require detailed surface representation or feature-based evaluation beyond conventional dimensional verification.

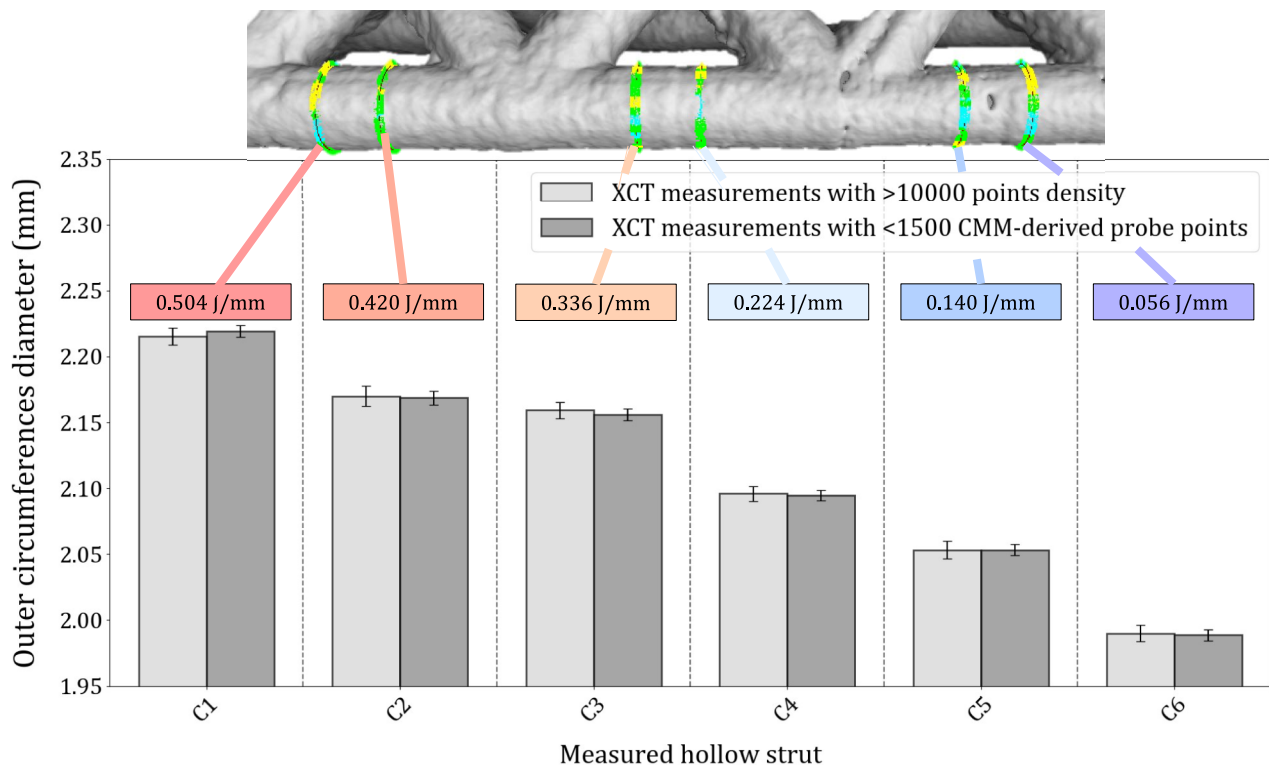


Fig. 8 Outer diameter measurements of hollow strut lattices obtained via XCT: (Step 1) using CMM-derived probe points (< 1500 points) and (Step 2) using high-density point data ($> 10,000$ points) for least-squares circumference fitting. Error bars represent U_{MP}

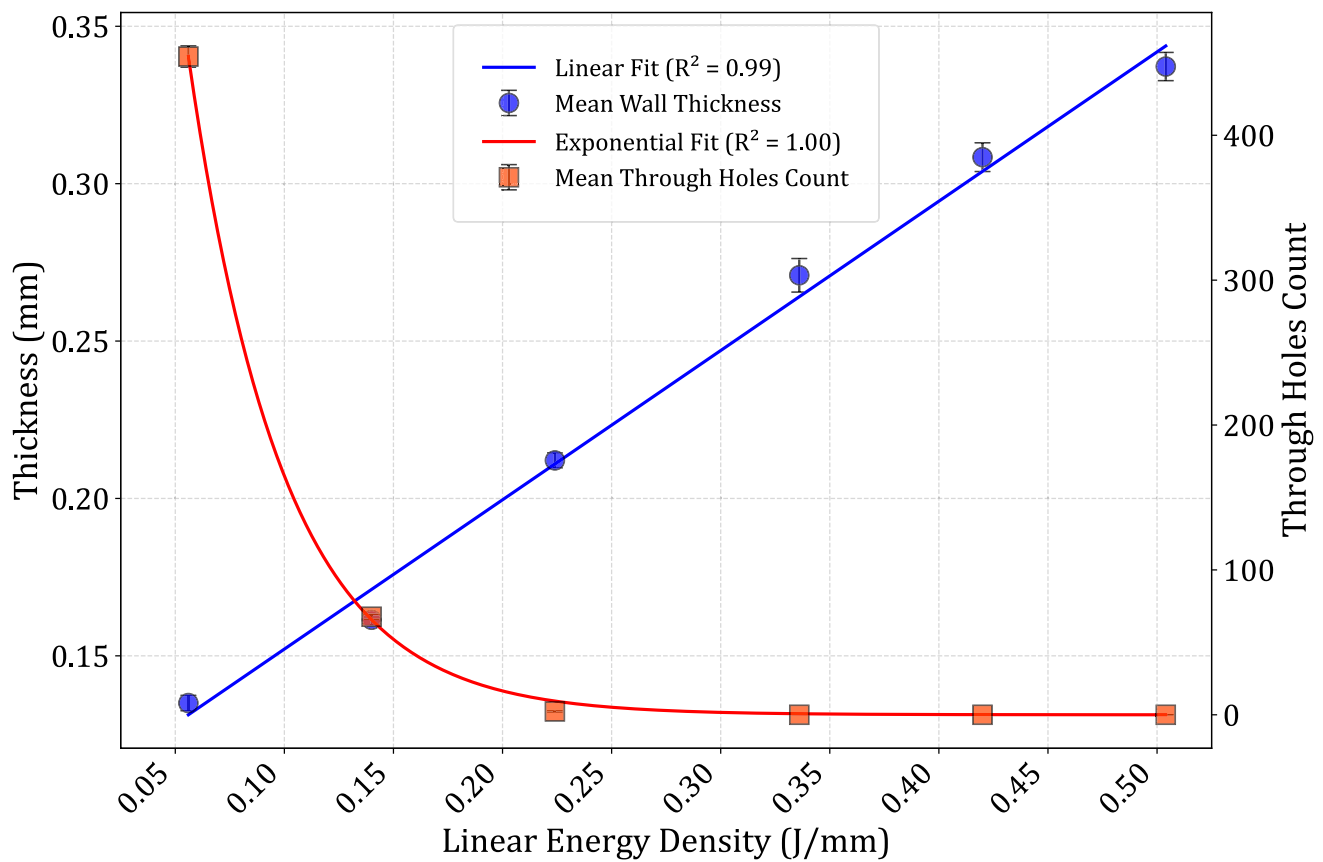


Fig. 9 Primary axis: mean wall thickness for each LED; secondary axis: Mean number of through-holes detected in MM1

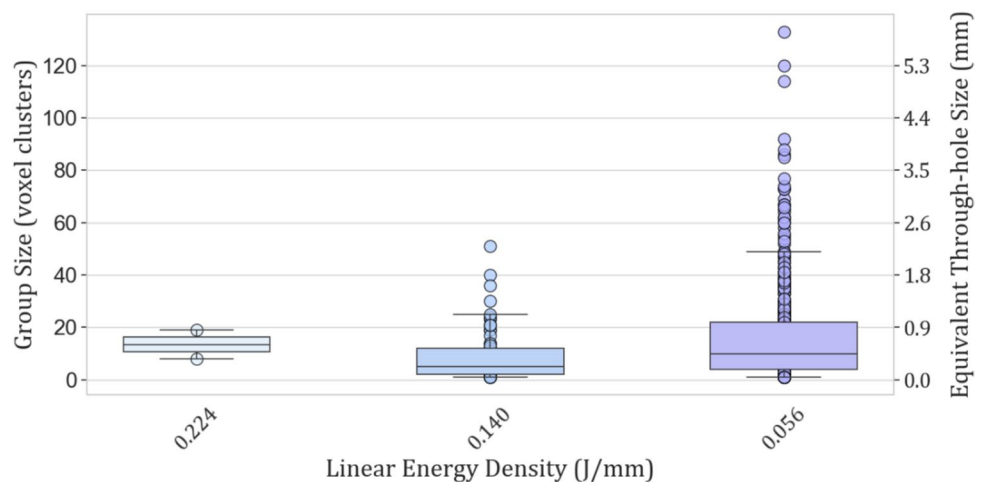
3.2 Influence of Laser LED on Wall Thickness and Through-Hole Formation Using XCT

Following the assessment of measurement uncertainties for the outer diameters of the material measure MM1 corner hollow strut, the mean wall thickness and through-hole detection, as detailed in Sections 2.2 and 2.3, were analyzed. Figure 9 illustrates the mean wall thickness (primary axis)

and the mean number of through-holes detected (secondary axis) across five XCT scan repetitions, with bars representing standard deviation of the repeated measurement values.

The LED values shown correspond to six discrete LED regions, each fabricated with a fixed and pre-defined laser energy input. These values were selected to cover representative under- and over-melting conditions, not to define a continuous parameter spectrum. The observed trends are

Fig. 10 Mean through-hole size detected in MM1 for each LED region, based on the first XCT scan repetition. Error bars represent the standard deviation of through-hole sizes within each region. The secondary axis shows the equivalent physical size in micrometers based on a 44 μm voxel size



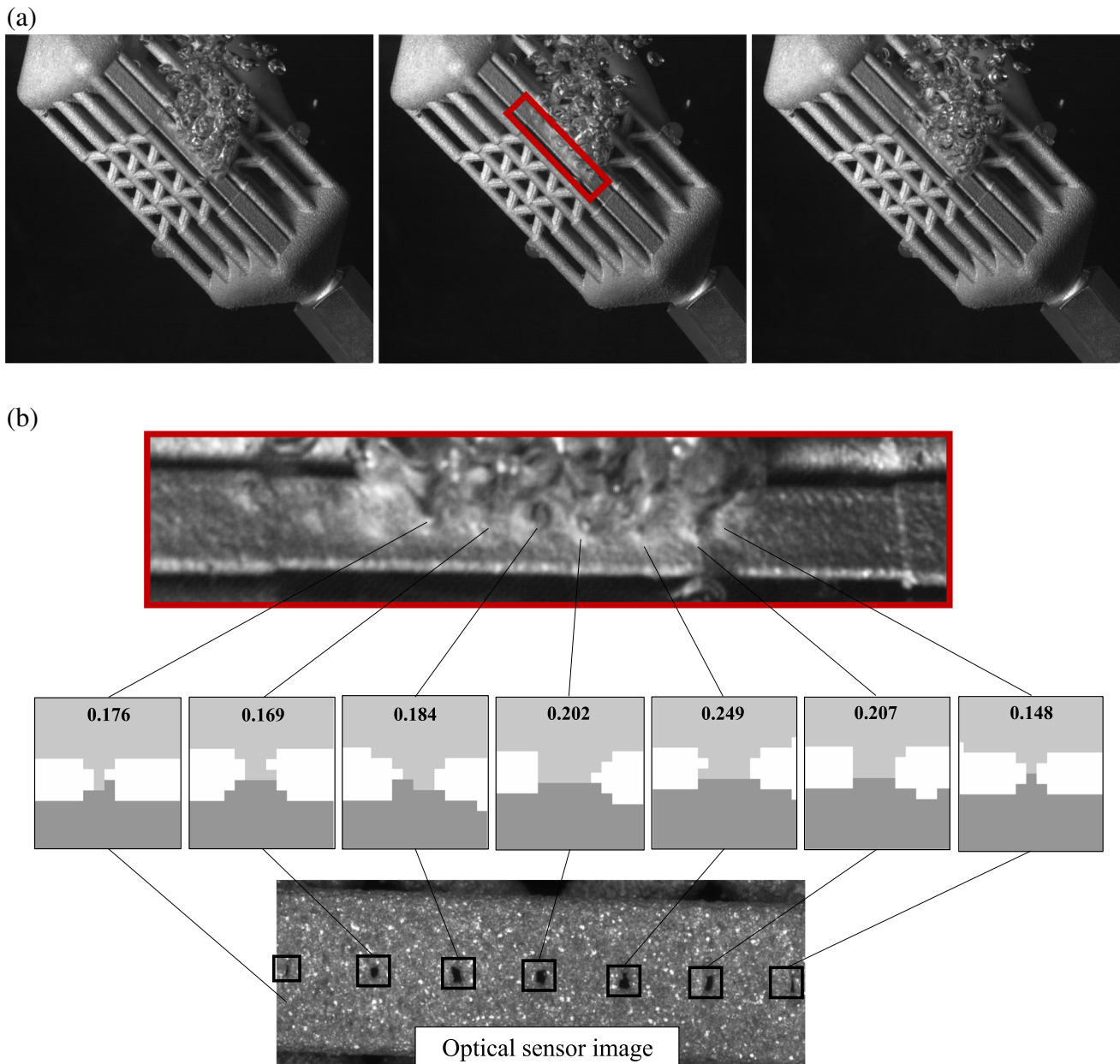


Fig. 11 (a) Selected frames from high-speed camera recordings of CAD-designed through-holes during the leakage test of MM2—full video is included as supplementary material. (b) Corresponding

XCT-detected through-holes using the proposed algorithm, where the numbers indicate the calibrated through-hole diameters in mm, alongside the reference optical sensor image

therefore representative of this discrete dataset and are not intended to imply continuity across the full LED spectrum.

A linear relationship was identified between increasing LED and mean wall thickness, while the number of through-holes decreased exponentially. The exponential fitting was selected based on both statistical performance and physical reasoning. From a quantitative standpoint, the exponential model provided the highest coefficient of determination (R^2) among the tested models (linear and polynomials), indicating the best agreement with the experimental data. From

a process physics perspective, this behavior is consistent with the defect formation mechanisms in PBF-LB: as LED decreases below a critical threshold, LoF defects and incomplete melting rapidly increase, resulting in a non-linear, accelerated rise in through-hole occurrence [39].

Under-melting conditions resulted in mean wall thicknesses ranging from 0.135 mm to 0.212 mm, significantly below the nominal 0.3 mm, with consistent through-hole formation. Over-melting conditions eliminated through-holes entirely, as the elevated energy input increased both

porosity and wall thickness proportionally. Variability in through-hole detection across repetitions was minimal, with a maximum variation of 5% observed in lower energy density regions where the through-hole population was higher.

Figure 10 presents the mean size of process-induced through-holes detected by the multi-step XCT algorithm in MM1, calculated as the number of contiguous voxels forming each connected defect cluster during the final intersection step of the procedure (see Step 3 in Fig. 6). The analysis is based on a single XCT scan repetition to maintain visual clarity. Error bars indicate the standard deviation of through-hole sizes within each LED region.

Results show that more than 80% of the detected through-holes exceed the 4×4 voxel threshold ($176 \mu\text{m}$), and over 90% exceed the 2×2 voxel threshold ($88 \mu\text{m}$). This supports that the vast majority of detected through holes fall within the reliably detectable range based on established XCT metrology guidelines and leakage test comparison results. Consistent with prior work by the authors [36], investigations at smaller voxel sizes have demonstrated that, when the 4×4 voxel criterion for reliable detection is maintained, the trend in measurement uncertainty remains stable across resolutions. This evidence reinforces the expectation that the relationships and conclusions reported in the present study would remain applicable at finer voxel sizes. The results suggest that within the under-melting energy density range, laser LED does not significantly affect the mean through-hole size. The formation of through-holes is primarily caused by incomplete fusion between adjoining welds due to suboptimal interaction between laser power and scan speed parameters. Although LED provides a general measure of processing conditions, specific combinations of laser power and scan speed more critically influence defect size [40], which is beyond the scope of this study.

Figure 11 displays XCT cross-sections of CAD-designed through-holes detected by the proposed XCT algorithm, alongside a high-speed camera images obtained during the leakage test of MM2. The results validate the effectiveness of the XCT detection algorithm, which successfully identified all CAD-designed through-holes. A video is included as supplementary material, to demonstrate the leakage behavior of CAD-designed through-holes observed during the high-speed camera test shown in Fig. 11.

4 Conclusions

This study demonstrates the effectiveness of XCT as a metrological tool for analyzing hollow lattice structures produced via PBF-LB. A novel XCT-based algorithm for automated through-hole detection was developed and validated through leakage tests, confirming its reliability in detecting through-holes across various geometries and sizes.

The substitution method, adapted from ISO 15530–3 for tactile CMMs, was used to evaluate XCT measurement uncertainties for hollow lattice dimensions. Two measurement methods were compared: (1) based on the probe points used for CMM calibration and (2) derived from high-density point data. While the measurement uncertainty in method 2 was higher than that of method 1, it remained within the specified tolerance and allowed for detailed capture of fine surface features. Key results highlight a trade-off between minimizing wall thickness and through-hole formation. Under-melting conditions yielded wall thicknesses of 0.135 mm to 0.212 mm , significantly below the nominal 0.3 mm , but resulted in an exponential increase in through-hole occurrence. Conversely, a linear correlation was observed between increasing energy density and wall thickness, with over-melting conditions eliminating through-holes entirely.

Future work will focus on quantifying the measurement uncertainties associated with through-hole count and dimensions, and on extending the methodology to other thin-walled configurations prone to through-hole formation, including the evaluation of voxel size influence on these measurements. In addition, although a local iterative function was used for surface determination in the XCT scans, different surface determination algorithms and parameter settings on the dimensional and form error measurements of through-holes deserves further investigation to assess their potential impact on measurement accuracy.

Supplementary Information The online version contains supplementary material available at <https://doi.org/10.1007/s10921-025-01269-8>.

Acknowledgements The authors extend their sincere gratitude to the reviewers of this paper for their thoughtful and meticulous feedback. Their insightful comments, constructive critiques, and valuable observations have played a pivotal role in refining and enhancing the quality of this manuscript.

Author Contribution I.H. was responsible for conceptualization, methodology development, formal analysis, investigation, and drafting of the original manuscript. N.O. contributed to conceptualization, funding acquisition, supervision, validation, and manuscript review and editing. J.A.Y.-F. contributed to project administration, supervision, validation, and manuscript review and editing. S.P. contributed to resource provision and manuscript review and editing. H.V.-G. was involved in conceptualization, supervision, validation, and manuscript review and editing. All authors reviewed and approved the final version of the manuscript.

Funding Open Access funding provided thanks to the CRUE-CSIC agreement with Springer Nature. This work was funded by the MICIU/AEI/ <https://doi.org/10.13039/501100011033> and by FEDER, UE, under Grant Number PID2024-160031OB-I00. This work was also funded by the Basque Government's Department of Industry, Energy Transition, and Sustainability under Grant Number KK-2024/00080 and Grant Number KK-2025/00068. This research also received some help from Basque Government by university research groups, grant IT1573-22.

Data Availability The data supporting the findings of this study are available from the authors upon reasonable request.

Declarations

Competing interests The authors declare no competing interests.

Open Access This article is licensed under a Creative Commons Attribution 4.0 International License, which permits use, sharing, adaptation, distribution and reproduction in any medium or format, as long as you give appropriate credit to the original author(s) and the source, provide a link to the Creative Commons licence, and indicate if changes were made. The images or other third party material in this article are included in the article's Creative Commons licence, unless indicated otherwise in a credit line to the material. If material is not included in the article's Creative Commons licence and your intended use is not permitted by statutory regulation or exceeds the permitted use, you will need to obtain permission directly from the copyright holder. To view a copy of this licence, visit <http://creativecommons.org/licenses/by/4.0/>.

References

- Ha, N.S., Lu, G.: A review of recent research on bio-inspired structures and materials for energy absorption applications. *Composites Part B: Engineering* **181**, 107496 (2020). <https://doi.org/10.1016/j.compositesb.2019.107496>
- Sullivan, T.N., Wang, B., Espinosa, H.D., Meyers, M.A.: Extreme lightweight structures: avian feathers and bones. *Mater. Today* **20**, 377–391 (2017). <https://doi.org/10.1016/j.mattod.2017.02.004>
- Noronha, J., Dash, J., Leary, M., Downing, D., Kyriakou, E., Brandt, M., Qian, M.: Node-reinforced hollow-strut metal lattice materials for higher strength. *Scripta Mater.* **234**, 115547 (2023). <https://doi.org/10.1016/j.scriptamat.2023.115547>
- Yamada, S., Suzuki, H., Sawada, K., Okada, S., Nishimura, A., Todoh, M.: Novel strut-based stochastic lattice biomimetically designed based on the structural and mechanical characteristics of cancellous bone. *Mater. Des.* **251**, 113657 (2025). <https://doi.org/10.1016/j.matdes.2025.113657>
- Khan, N., Riccio, A.: A systematic review of design for additive manufacturing of aerospace lattice structures: current trends and future directions. *Progress in Aerospace Sciences* **149**, 101021 (2024). <https://doi.org/10.1016/j.paerosci.2024.101021>
- Redaccion, Trabajos en altura, Aisl. Rehabil. Edificios ARE (2020). <https://arefachadas.es/trabajos-en-altura/> (accessed August 8, 2025).
- Hurtado, M., Vallejo, B., Torres, C., Mantilla, A., González Escudero, M.: Influencia de surfactantes en la evaluación de la tensión interfacial para una emulsión agua petróleo relacionada al proceso de recuperación mejorada, FIGEMPA Investig. Desarro **1**, 9–14 (2017). <https://doi.org/10.29166/revfig.v1i2.1559>
- What is generative design in architecture and construction?, (n.d.). <https://www.autodesk.com/design-make/articles/generative-design-architecture> (accessed August 8, 2025).
- Eddie Nahúm, A.-M., Carbo, P., Bocanegra, C., Lopez Hernandez, J., Peña, E., Rocha-Rangel, E., García, J.: Ingeniería Bioinspirada, 2014. <https://doi.org/10.3926/oms.235>
- Wang, Z., Dubrowski, A.: A semi-automatic method to create an affordable three-dimensional printed splint using open-source and free software. *Cureus* **13**, e13934 (2021). <https://doi.org/10.7759/cureus.13934>
- Zhou, Y., Shen, S., Liu, T., Li, P., Duan, F.: Effective heat conduction evaluation of lattice structures from selective laser melting printing. *International Journal of Heat and Mass Transfer* **218**, 124790 (2024). <https://doi.org/10.1016/j.ijheatmasstransfer.2023.124790>
- Kaur, I., Aider, Y., Nithyanandam, K., Singh, P.: Thermal-hydraulic performance of additively manufactured lattices for gas turbine blade trailing edge cooling. *Appl. Therm. Eng.* **211**, 118461 (2022). <https://doi.org/10.1016/j.applthermaleng.2022.118461>
- Narkhede, S., Sur, A.: Performance prediction of hollow micro-lattice cross-flow heat exchanger using a numerical approach. *International Journal of Ambient Energy* **43**, 4909–4916 (2022). <https://doi.org/10.1080/01430750.2021.1927835>
- Zhong, H.Z., Song, T., Li, C.W., Das, R., Gu, J.F., Qian, M.: Understanding the superior mechanical properties of hollow-strut metal lattice materials. *Scripta Mater.* **228**, 115341 (2023). <https://doi.org/10.1016/j.scriptamat.2023.115341>
- de Damborenea, J., Conde, A., Gardon, M., Ravi, G.A., Arenas, M.A.: Effect of growth orientation and heat treatment on the corrosion properties of AISi10Mg alloy produced by additive manufacturing. *J. Mater. Res. Technol.* **18**, 5325–5336 (2022). <https://doi.org/10.1016/j.jmrt.2022.05.021>
- Noronha, J., Leary, M., Brandt, M., Qian, M.: AISi10Mg hollow-strut lattice metamaterials by laser powder bed fusion. *Mater. Adv.* **5**, 3751–3770 (2024). <https://doi.org/10.1039/D3MA00813D>
- Wang, J., Zhu, R., Liu, Y., Zhang, L.: Understanding melt pool characteristics in laser powder bed fusion: an overview of single- and multi-track melt pools for process optimization. *Advanced Powder Materials* **2**, 100137 (2023). <https://doi.org/10.1016/j.apmate.2023.100137>
- Nayak, S.K., Mishra, S.K., Paul, C.P., Jinoop, A.N., Bindra, K.S.: Effect of energy density on laser powder bed fusion built single tracks and thin wall structures with 100 µm preplaced powder layer thickness. *Optics & Laser Technology* **125**, 106016 (2020). <https://doi.org/10.1016/j.optlastec.2019.106016>
- Zhang, L., Lifton, J., Hu, Z., Hong, R., Feih, S.: Influence of geometric defects on the compression behaviour of thin shell lattices fabricated by micro laser powder bed fusion. *Addit. Manuf.* **58**, 103038 (2022). <https://doi.org/10.1016/j.addma.2022.103038>
- Snow, Z., Scime, L., Ziabari, A., Fisher, B., Paquit, V.: Observation of spatter-induced stochastic lack-of-fusion in laser powder bed fusion using in situ process monitoring. *Additive Manufacturing* **61**, 103298 (2023). <https://doi.org/10.1016/j.addma.2022.103298>
- Schwerz, C., Raza, A., Lei, X., Nyborg, L., Hryha, E., Wirdelius, H.: In-situ detection of redeposited spatter and its influence on the formation of internal flaws in laser powder bed fusion. *Addit. Manuf.* **47**, 102370 (2021). <https://doi.org/10.1016/j.addma.2021.102370>
- Bonato, N., Zanini, F., Carmignato, S.: Prediction of spatter-related defects in metal laser powder bed fusion by analytical and machine learning modelling applied to off-axis long-exposure monitoring. *Addit. Manuf.* **94**, 104504 (2024). <https://doi.org/10.1016/j.addma.2024.104504>
- Barros, R., Silva, F.J.G., Gouveia, R.M., Saboori, A., Marchese, G., Biamino, S., Salmi, A., Atzeni, E.: Laser powder bed fusion of Inconel 718: residual stress analysis before and after heat treatment. *Metals* **9**, 1290 (2019). <https://doi.org/10.3390/met9121290>
- Zanini, F., Bonato, N., Michieletto, D., Alberti, L., Carmignato, S.: Laser powder bed fusion process optimization for the production of high-performance and efficient high-silicon steel electrical motor components. *Prog. Addit. Manuf.* **10**, 6581–6592 (2025). <https://doi.org/10.1007/s40964-025-00993-x>
- Li, C., Liu, Z.Y., Fang, X.Y., Guo, Y.B.: Residual stress in metal additive manufacturing. *Procedia CIRP* **71**, 348–353 (2018). <https://doi.org/10.1016/j.procir.2018.05.039>
- Dewulf, W., Bosse, H., Carmignato, S., Leach, R.: Advances in the metrological traceability and performance of X-ray computed

- tomography. *CIRP Annals* **71**, 693–716 (2022). <https://doi.org/10.1016/j.cirp.2022.05.001>
27. Villarraga-Gómez, H., Herazo, E.L., Smith, S.T.: X-ray computed tomography: from medical imaging to dimensional metrology. *Precis. Eng.* **60**, 544–569 (2019). <https://doi.org/10.1016/j.precisioneng.2019.06.007>
 28. Noronha, J., Leary, M., Qian, M., Kyriakou, E., Brandt, M.: Geometrical parameters and mechanical properties of Ti6Al4V hollow-walled lattices. *Mater. Sci. Eng. A* **840**, 142667 (2022). <https://doi.org/10.1016/j.msea.2022.142667>
 29. Shi, X., Liu, X., Ren, S., Lu, P., Xie, Z., Wu, M.: Selective laser melting fabricated tungsten with thin-walled structure: role of linear energy density on temperature evolution and manufacturing quality. *Int. J. Mater. Form.* **15**, 2 (2022). <https://doi.org/10.1007/s12289-021-01646-4>
 30. European Cooperation for Accreditation, Evaluation of the uncertainty of measurement in calibration (EA-4/02 M:2022), 2022.
 31. Sun, W., Giusca, C., Lou, S., Yang, X., Chen, X., Fry, T., Jiang, X., Wilson, A., Brown, S., Boulter, H.: Establishment of X-ray computed tomography traceability for additively manufactured surface texture evaluation. *Additive Manuf.* **50**, 102558 (2022). <https://doi.org/10.1016/j.addma.2021.102558>
 32. VDI/VDE 2630 Part 2.1 (2015) Computed tomography in dimensional measurement – Determination of the uncertainty of measurement and the test process suitability of coordinate measurement systems with CT sensors
 33. Zanini, F., Sorgato, M., Savio, E., Carmignato, S.: Dimensional verification of metal additively manufactured lattice structures by X-ray computed tomography: use of a newly developed calibrated artefact to achieve metrological traceability. *Additive Manufacturing* **47**, 102229 (2021)
 34. Geometrical product specifications (GPS). Coordinate measuring machines (CMM). Technique for determining the uncertainty of measurement. Part 3: Use of calibrated workpieces or measurement standards (ISO 15530–3:2011), 2011
 35. Townsend, A., Pagani, L., Blunt, L., Scott, P.J., Jiang, X.: Factors affecting the accuracy of areal surface texture data extraction from X-ray CT. *CIRP Annals* **66**, 547–550 (2017). <https://doi.org/10.1016/j.cirp.2017.04.074>
 36. Holgado, I., Ortega, N., Yagüe-Fabra, J.A., Plaza, S., Villarraga-Gómez, H.: Metrological evaluation and classification of porosity in metal additive manufacturing using X-ray computed tomography. *Mater. Des.* **254**, 114057 (2025). <https://doi.org/10.1016/j.matdes.2025.114057>
 37. Schild, L., Weiser, L., Höger, K., Lanza, G.: Analyzing the error of computed tomography-based pore detection by using microscope images of matched cross-sections. *Precis. Eng.* **81**, 192–206 (2023). <https://doi.org/10.1016/j.precisioneng.2023.01.013>
 38. Lifton, J., Liu, T.: An adaptive thresholding algorithm for porosity measurement of additively manufactured metal test samples via X-ray computed tomography. *Addit. Manuf.* **39**, 101899 (2021). <https://doi.org/10.1016/j.addma.2021.101899>
 39. Mojumder, S., Gan, Z., Li, Y., Amin, A.A., Liu, W.K.: Linking process parameters with lack-of-fusion porosity for laser powder bed fusion metal additive manufacturing. *Additive Manufacturing* **68**, 103500 (2023). <https://doi.org/10.1016/j.addma.2023.103500>
 40. Leung, C.L.A., Marussi, S., Atwood, R.C., Towrie, M., Withers, P.J., Lee, P.D.: In situ X-ray imaging of defect and molten pool dynamics in laser additive manufacturing. *Nat. Commun.* **9**, 1355 (2018). <https://doi.org/10.1038/s41467-018-03734-7>

Publisher's Note Springer Nature remains neutral with regard to jurisdictional claims in published maps and institutional affiliations.